

Spatially regulated water-heat transport by fluidic diode membrane for efficient solar-powered desalination and electricity generation

Received: 2 January 2025

Accepted: 14 May 2025

Published online: 30 May 2025

Yuanhang Cao^{1,7}, Jiemin Wang^{1,7}✉, Weixin Guan², Meng An³✉, Peng Yan⁴, Zhengtong Li⁵, Changsheng Zhao⁶✉ & Guihua Yu²✉

Interfacial solar-driven evaporation has attracted great research interests, given its high conversion efficiency of solar energy and transformative industrial potential for desalination. However, current evaporators with porous volume remain critical challenges by inherently balancing efficient fluid transport and effective heat localization. Herein, we propose the strategy and design of lightweight, flexible and monolayered fluidic diode membrane-based evaporators, featuring regularly arrayed macropores and dense nanopores on each side. Such a delicate microstructure offers universality in establishing asymmetric channels along macroporous-to-nanoporous to enable the diode-like directional water transport as well as facilitate the heat localization on the nanopores side. Consequently, a high evaporation rate of a maximum $3.82 \text{ kg m}^{-2} \text{ h}^{-1}$ can be achieved under 1 sun illumination, exceeding most 2D and 3D evaporators. Besides, the durability and practicability of our evaporators are validated through salt resistance tests, purification experiments among various contaminants, and outdoor evaluations. Moreover, the structure engineering and water-transport optimization of fluidic diode membranes also offer potentials for hydrovoltaic applications, with over 1.6 V generated by tandem devices at the ambient environment. This work provides a concept for designing high-performance monolayered membranes applicable in environmental and energy-related realms.

Interfacial solar water evaporation (ISE) offers a promising pathway to address water scarcity by utilizing solar energy for decentralized water purification^{1–5}. This renewable and sustainable technology achieves evaporation at the air–water interface, minimizing thermal losses to

the bulk liquid and supporting diverse applications such as desalination and wastewater treatment^{6–10}. Among the various designs of ISE systems, membrane-based evaporators have garnered significant attention due to their unique capabilities in enhancing evaporation

¹College of Biomedical Engineering, Sichuan University, Chengdu, China. ²Materials Science and Engineering Program and Walker Department of Mechanical Engineering, The University of Texas at Austin, Austin, TX, USA. ³Yangtze Delta Region Academy in Jiaxing, Beijing Institute of Technology, JiaXing, China.

⁴College of Mechanical and Electrical Engineering, Shaanxi University of Science and Technology, Xi'an, China. ⁵State Key Laboratory of Hydrology-Water Resources and Hydraulic Engineering, Hohai University, Nanjing, China. ⁶College of Polymer Science and Engineering, State Key Laboratory of Polymer Materials Engineering, Sichuan University, Chengdu, China. ⁷These authors contributed equally: Yuanhang Cao, Jiemin Wang. ✉ e-mail: jiemin@scu.edu.cn; anmeng@photon.t.u-tokyo.ac.jp; zhaochsh70@scu.edu.cn; ghyu@austin.utexas.edu

efficiency. Membrane evaporators distinguish themselves by their inherently short water transport distance, which facilitates rapid replenishment of water to the evaporation interface. Additionally, membranes exhibit scalability and adaptability, making them attractive for large-scale water purification applications^{11–14}. However, despite these advantages, the performance of membrane evaporators is often constrained by a critical trade-off: balancing efficient water transport with effective heat localization. Generally, achieving high water flux requires a highly porous and hydrophilic structure, yet such designs can lead to increased heat dissipation, undermining the thermal efficiency essential for interfacial evaporation^{15,16}. This trade-off becomes particularly pronounced when comparing membrane evaporators with alternative designs. Conventional monolayered membranes typically feature dense nanopores across both surfaces, which significantly limit water permeability and hinder efficient transport (Fig. 1a)^{17,18}. In contrast, through-hole monolayered membranes, such as ordered porous and textile membranes, improve water uptake by enabling more direct transport pathways. However, this enhancement comes at the cost of reduced surface area for light absorption and heat localization, which are critical for maximizing evaporation efficiency (Fig. 1b)^{19–21}.

To address this challenge, we propose a gradient pore membrane design that leverages spatial variations in pore size and wettability to optimize water transport and heat management (Fig. 1c). By integrating a hierarchical structure, the gradient pore membrane directs water efficiently to the evaporation interface while maintaining localized heat confinement, overcoming the limitations of uniform pore structures. This design concept is elaborated by simple models referring to gradient pores and homogeneous pores that are built through molecular dynamics (MD) simulations (Fig. 1d, Supplementary Movie S1 and Method S1). The results indicate that the water molecules can spontaneously traverse the gradient pore channels from the larger pore to the smaller pore within 20 ns (Fig. 1e). Yet, this process is difficult to realize in both homogenous pore channels and reverse gradient pores. It is ascribed to the ratchet effect of molecular transport in confined channels^{22,23}. In this scenario, the entropic barrier, an essential component of the ratchet effect, can stem from asymmetric potential induced by gradient pores from large size to small size. The large negative pressure in the gradient pore rather than the homogenous pore enables the absorption of water molecules (Fig. 1f). Thus, the asymmetrical gradient pore structure is promising for inducing the water directional transport and establishes a Janus structure in the monolayered membranes with a diode-like effect for boosting ISE (Fig. 1g).

Herein, a phase-separation combined with template assembly (PCTA) strategy is developed to fabricate superstructured monolayered fluidic diode membranes (FDMs). These FDMs feature regularly arrayed macropores on one side, dense nanopores on the other, and gradient pores across their thickness. This pronounced structural asymmetry effectively balances the trade-off between water supply and heat localization in conventional membranes. Consequently, key properties, including directional water transport, solar evaporation performance, and salt resistance, are significantly enhanced. For example, under 1 sun illumination, the FDMs-based evaporator operating along the macroporous-to-nanoporous direction achieves at least 40% enhancement of evaporation rate compared to conventional membrane cases, as well as outperforms many state-of-the-art designs. Besides, a high evaporation rate of a maximum $3.82 \text{ kg m}^{-2} \text{ h}^{-1}$ can be achieved under a three-dimensional (3D) configuration. Furthermore, the revealed structure-function relationship also improves hydrovoltaic electricity generation, expanding its potential for power output. This work provides a versatile design framework for monolayered membrane structures, advancing solar desalination and hydrovoltaic applications.

Results

Fabrication and characterization of FDMs

The fabrication of the FDMs was enabled by a scalable PCTA strategy (Fig. 2a). Briefly, the polymer solution was spread on a silicon wafer with an array of cylindrical micropatterns (Supplementary Fig. S1), followed by spin-coating to ensure uniform distribution. Afterwards, the coated template was immersed in a coagulation bath to induce the phase separation of the polymer matrix. Finally, the freestanding FDMs were formed after peeling from the template. Noticeably, the thickness and morphology can be well-tuned by the coating speed, time, and viscosity (Supplementary Fig. S2 and Table S1). The PCTA strategy can produce large-scale FDMs by increasing the template size (Supplementary Fig. S3). In this work, by modulating the precursors, we achieved two types of FDMs, both featuring regularly arrayed macropores and dense nanopores on their surfaces, but with distinct internal pore structures: FDM-1 exhibited finger-like gradient pores, while FDM-2 presented sponge-like gradient pores. For comparison, common monolayered membranes (CMMs) without superstructures were also prepared by ordinary phase separation, named as CMM-1 and CMM-2 accordingly. More details of morphology were shown in scanning electron microscope (SEM) images (Fig. 2b, c and Supplementary Figs. S4 and S5). On the array-pore side (A), the array macropores with a diameter of $20 \mu\text{m}$ were orderly arranged. Magnification of a single array macropore revealed abundant secondary pores ($\sim 1\text{--}2 \mu\text{m}$), forming hierarchically porous structures. Noticeably, compared with FDM-1, such secondary pores were also distributed on the A side of FDM-2, indicating a higher porosity due to a slower phase-separation process^{24,25}. Furthermore, the cross-sections of the FDMs revealed gradient pores ranging from macroporous to nanoporous features from top to bottom within an integrated membrane. Therefore, the FDM-1 reflected the finger-like pores with a transition from large cavities to narrow apertures, whereas the FDM-2 presented sponge-like pores with gradually changing pore size, hence interpreting a more continuous architecture. On the dense side (D), both the FDMs showed dense and compact surfaces with nanopores (Supplementary Fig. S6), similar to the CMMs (Supplementary Figs. S7 and S8). The depth of the array-pores in FDMs was further measured through an optical 3D surface profiler (Fig. 2d). The macropores were regular and uniform with a pore diameter of $20 \mu\text{m}$ and depth of $15 \mu\text{m}$, which greatly increased the surface roughness on A. We also investigated the optimal topology by preparing a series of FDMs with different array-pore sizes. When fabricating the FDM with a smaller $10 \mu\text{m}$ array-pore (Supplementary Fig. S9), the macropores were fragile and easily dislocated by the slim template pillars during peeling, leaving the pore shapes irregular. In contrast, the FDMs with $50 \mu\text{m}$ and $100 \mu\text{m}$ array-pore tended to present variable and uneven secondary pores or holes inside the array-pore (Supplementary Figs. S10 and S11), owing to heterogeneous phase separation between template-patterned and interstitial regions. The $20 \mu\text{m}$ design achieved an optimal balance: it maintained structural uniformity and hierarchical porosity gradients while avoiding these fabrication-induced defects, ensuring high reproducibility across multiple fabrication batches. Compared to conventional phase separation or electrospinning methods that typically yielded homogeneous porosity or multilayered structures, the PCTA strategy enabled direct formation of monolithic membranes with through-thickness pore gradients as well as diverse wettability domains. This structural programmability hence circumvented the trade-off between hydraulic permeability and thermal confinement in conventional evaporators.

Diode-like water transport behavior of FDMs

To further specify the hierarchical pore phases throughout the membrane, we adopted micro-computed tomography (micro-CT) to enable the in-plane layer scanning (Fig. 2E). Taking FDM-1 as an example, we selected five layers from D side to A side (D \rightarrow A). The outcomes

showed a trend of decreased porosity and average pore size along this direction. (Fig. 2f, g), which embodied the pore gradients and structural heterogeneity. Despite such a superstructure, FDMs maintained good flexibility (Fig. 2h) and mechanical properties (Fig. 2i) as CMMs.

We also tested the ultrafiltration performance of the membranes. Compared with CMMs, the water fluxes of the FDMs were generally increased (Fig. 2j), with little bovine serum albumin retention ratio loss (Supplementary Fig. S12). Interestingly, for the asymmetric FDMs,

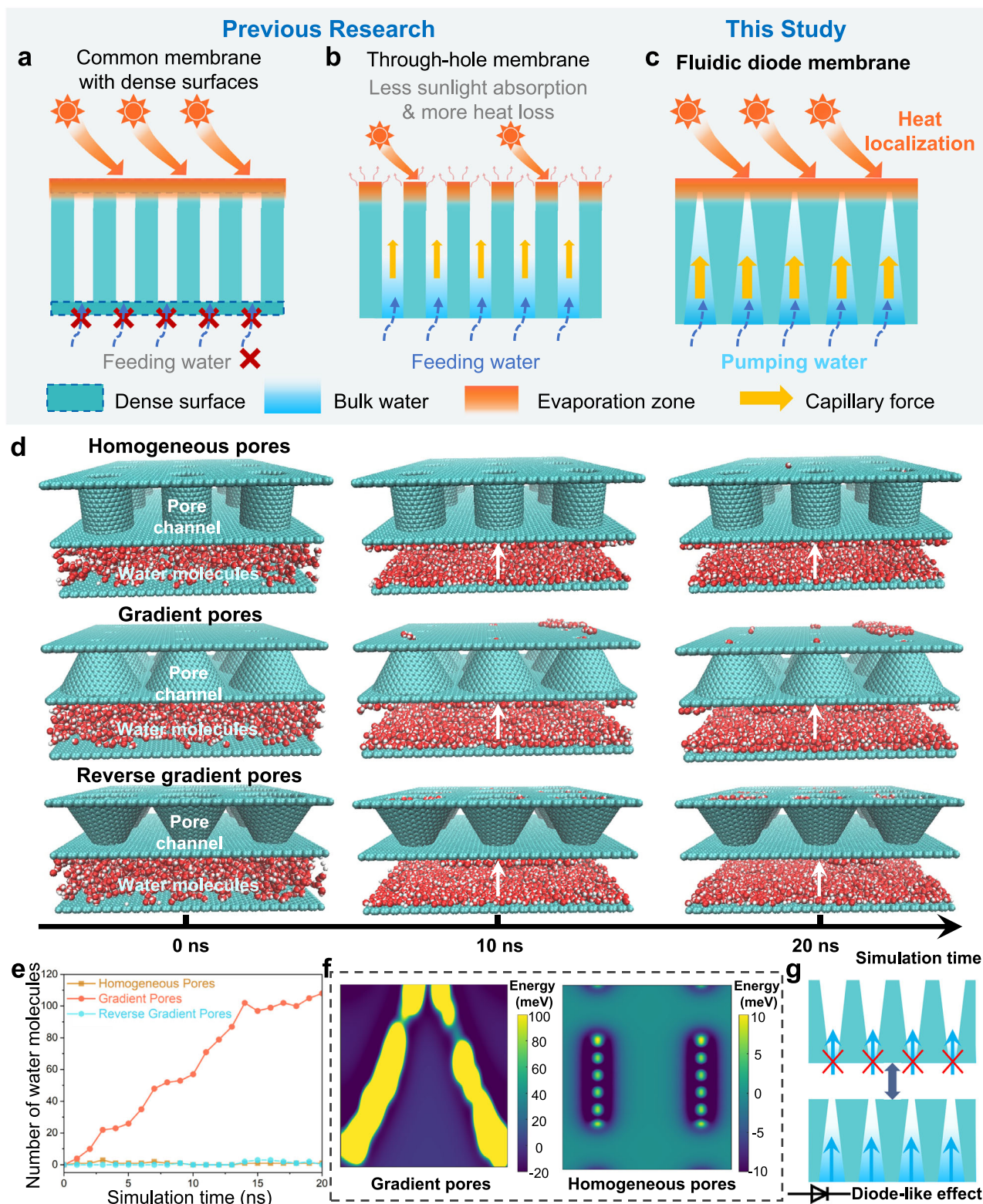


Fig. 1 | Concept of FDMs. a Common membrane. **b** Through-hole membrane, and **(c)** gradient-pore membrane in this study. **d** MD simulation of water molecules transport in homogeneous pores, gradient pores and reverse gradient pores. **e** The number of water molecules traversing the pore channels over simulation time.

f Potential energy distribution of gradient pores and homogeneous pores. **g** Schematic illustration of the diode-like effect of the gradient pore membrane. Source data are provided as a Source Data file.

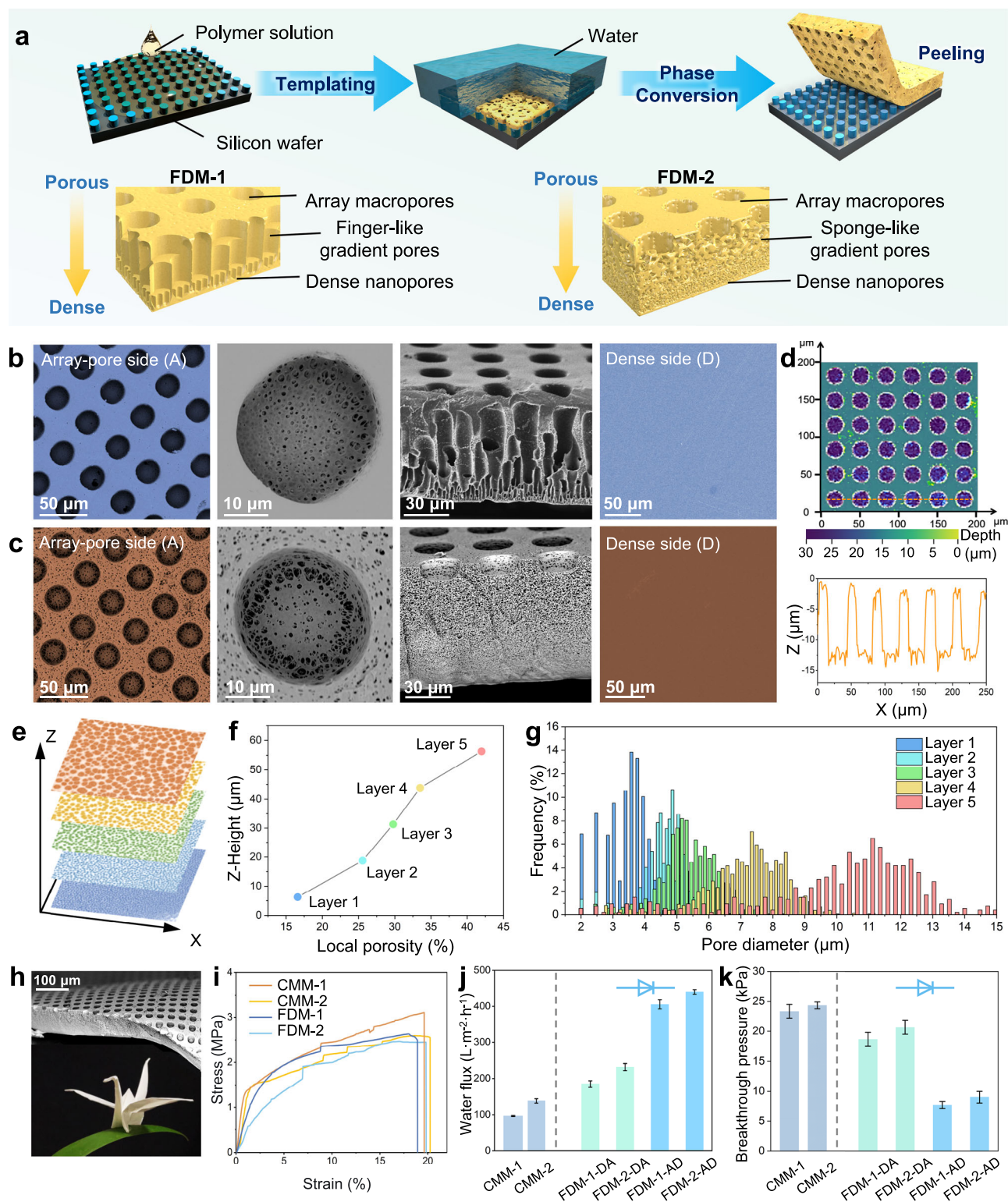


Fig. 2 | Fabrication and characterizations of FDMs. **a** Schematic illustration of the FDMs fabrication by PCTA. SEM images of **(b)** FDM-1 and **(c)** FDM-2 with both sides and cross-sections. **d** 3D surface micromorphology and depth profile of the FDM. **e** In-plane scanning images of FDMs from micro CT. **f** Local porosity and **(g)** Pore size distribution of different layers in FDM-1. **h** SEM image and photograph of the

FDM, showing the flexibility. **i** Tensile stress-strain curves of different membranes. **j** Water fluxes (1 bar at room temperature) and **(k)** breakthrough pressures of different membranes. Data are shown as mean \pm SD ($n = 3$ independent experiments). Source data is provided as a Source Data file.

when feeding water from A side to D side (marked as FDM-AD, AD was the water transport direction: A \rightarrow D), the water fluxes were approximately twice as high as those from the opposite direction (marked as FDM-DA). It therefore implied a diode-like effect of water permeability

in FDMs. We further measured the breakthrough pressures through a dead-end filtration cell. As shown in Fig. 2k, when water permeated along D \rightarrow A, the breakthrough pressures of the FDMs-DA were as high as ~ 20 kPa, close to those of the CMMs (~ 24 kPa). Conversely, they

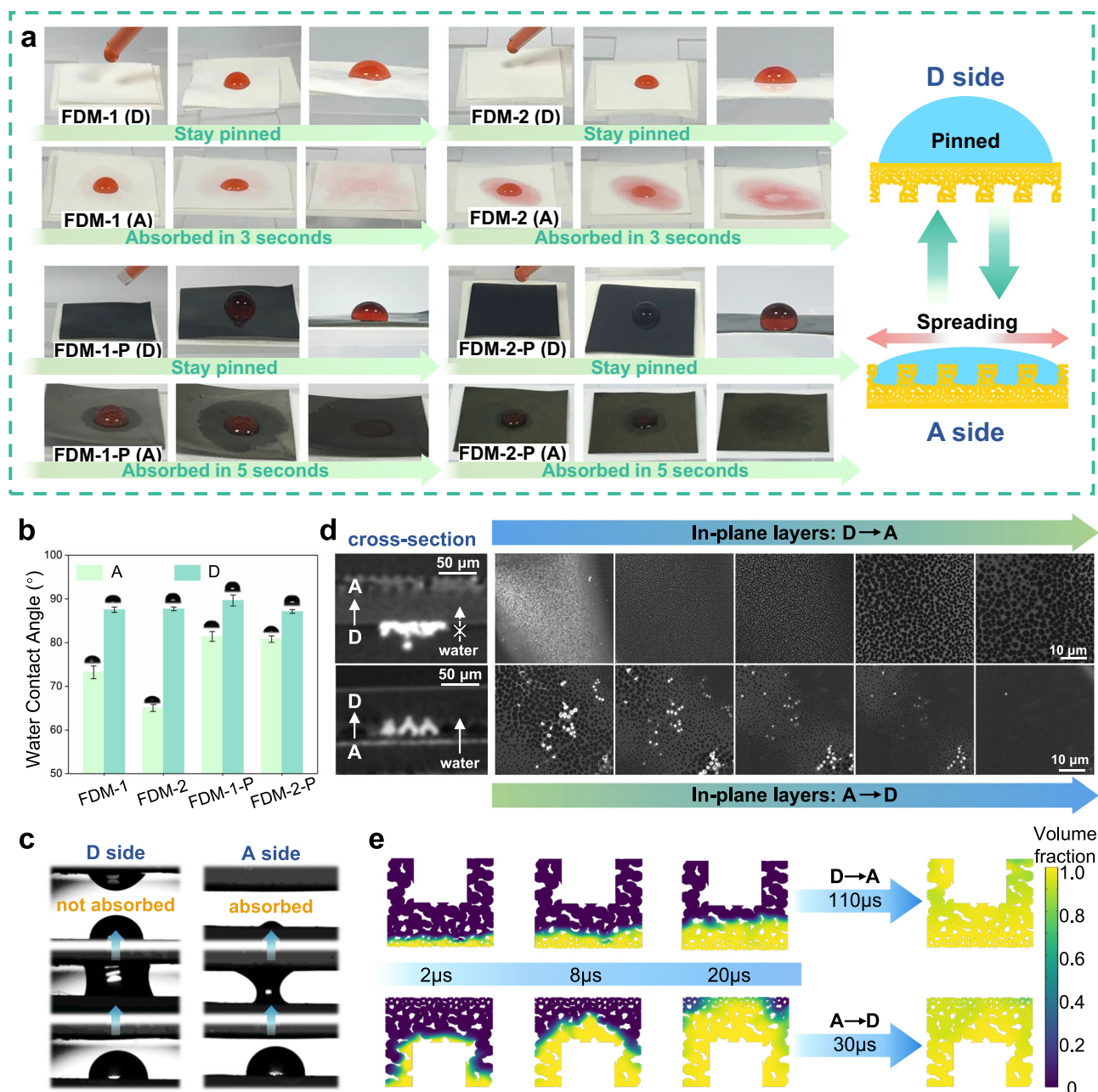


Fig. 3 | Water transport performance of membranes. **a** Wetting behaviors of water droplets on different sides of membranes. **b** Static water contact angles of FDMs. **c** Observation of anti-gravity water transport of FDMs. Data are shown as

mean \pm SD ($n = 3$ independent experiments). **d** Micro-CT images of cross-section and in-plane section of FDMs. **e** Numerical simulation results of water volume fraction distribution in FDMs. Source data are provided as a Source Data file.

dropped dramatically below 10 kPa along $A \rightarrow D$ for the FDMs-AD, which accounted for the diode-like effect of asymmetric water permeation.

To enable the photothermal property, we coated polypyrrole (Ppy) throughout the membranes via vapor-phase polymerization (Supplementary Fig. S13). The successful polymerization was confirmed by Fourier transform infrared spectra (FT-IR), X-ray photoelectron spectroscopy (XPS) and energy dispersive spectroscopy mapping (Supplementary Fig. S14–S16). Additionally, the as-obtained black membranes (FDMs-P) were stable, without damage under ultrasonic treatment in water (Supplementary Fig. S17). Notably, for ISE, water transport behaviors were essential. The factors, such as pore size, porosity, and pore distribution, profoundly influenced the water transport capability of membrane evaporators^{16,26}. Here, a red dye solution was dropped onto the surfaces of the membranes to observe

the wetting behaviors (Fig. 3a). When a droplet was deposited on the D side of the FDMs, it became pinned and remained steady. In contrast, when dropped on the A side, it rapidly spread and got absorbed within less than 3 seconds. Similar behaviors were observed in FDMs-P as well. However, for the CMMs and CMMs-P, the droplets were kept pinned on both sides (Supplementary Fig. S18). To further verify the asymmetric wettability, the water contact angles were measured. As shown in Fig. 3b and Supplementary Fig. S19, for all the FDMs and FDMs-P, the water contact angles on the D side were $\sim 90^\circ$, with a mere slight decrease in 300 s. On the contrary, the dynamic water contact angles on the A side dropped to 0° within ~ 2 seconds, indicating the improved wettability. Besides, although the introduction of Ppy as a solar absorber slightly reduced the hydrophilicity of FDM-1-P and FDM-2-P, their dynamic water contact angles still dropped to 0° within 4 seconds, and they also exhibited diode-like asymmetric water flux (Fig. S20).

It is worth noting that the FDMs consisted of homogeneous materials, but showcased disparate wetting behaviors on two sides. We attributed it to the asymmetrical structure that endowed the diode-like effect. As the simplified model in Fig. S21, when a droplet contacted the membrane, the droplet experienced a downward pressure P_H and an upward Laplace pressure P_L . The P_H was a constant related to the droplet height, while P_L increased with decreasing pore size^{16,27}. In our case, when a droplet landed on the nanopore of D side, the Laplace pressure P_L was higher than P_H , which impeded further downward permeation, and thus pinned the droplet. Conversely, when a droplet landed on the macropore of A side, the Laplace pressure P_L was low ($P_L < P_H$), allowing the liquid to pass through and spread out. Nevertheless, although the droplet can permeate beneath A side, it cannot fully penetrate the D side because of the increased P_H in the nanopores on the D side. The permeation accessible, yet non-penetration property facilitated the water confinement and kept the thermal concentration during ISE²⁸.

To further interpret the diode-like water transport capabilities, anti-gravity water transport experiments were carried out. The design of anti-gravity water transport tests can mimic the water transport upwards during photothermal evaporation. As shown in Fig. 3c and Movie S2–5, for both FDM-1 and FDM-2, upon contact with the A side, the water droplet was rapidly absorbed and infiltrated into the membrane. Oppositely, when the droplet touched the D side, no absorption and infiltration occurred. It thus reflected the diode-like water transport character macroscopically. Then, micro CT was employed to microscopically probe the water transport condition in the FDMs from either D → A (DA) or A → D (AD). A copper ion aqueous solution was prepared as a contrast agent to visualize the water upward absorption. When the aqueous solution passed through the membrane, the copper ions remained in some areas, leaving bright regions that were identified. As displayed in Fig. 3d, along D → A at the cross-section, the bright spots only accumulated on the surface of the D side, suggesting no water transport along this direction. Conversely, along A → D at the cross-section, distinct bright spots were observed within the membrane, thus unveiling the directional transport property. Besides, the scanned images of in-plane layers also reflected that the bright spots only appeared in the gradient pore layers along A → D, highlighting the diode-like water transport in FDMs. Numerical simulations were conducted to elaborate on the structural advantages of FDMs upon water transport (Fig. 3e, Supplementary Method S2, and Fig. S22). The symmetric structure was simplified to an orthogon ($40 \times 40 \mu\text{m}$) with non-gradient pores, whereas the asymmetric superstructure was modeled with a macropore ($20 \times 15 \mu\text{m}$) with hierarchically gradient pores. For a symmetric structure, it took 90 μs for water to completely infiltrate. By contrast, in the asymmetric superstructure, it took 30 μs and 110 μs for full permeation along A → D and D → A, respectively. It hence revealed that the superstructure of the FDMs not only induced the diode-like water transport, but also accelerated the water movement towards the evaporation interface. Taken together, the diode-like directional water transport mechanism of FDM was fundamentally rooted in its asymmetric macro-to-nanopore gradient. Spatial decoupling of water supply (macropores on A side) and evaporation interface (nanopores on D side) created distinct functional zones. The macro array-pores minimized hydraulic resistance for rapid water uptake, while the nanopores simultaneously facilitated capillary-driven unidirectional flow as well as establishing thermal confinement. This structural asymmetry thus reconciled the intrinsic contradiction between permeability and heat localization in conventional membranes.

ISE performances of FDMs

Next, we investigated the ISE performances of membrane evaporators. In terms of previous water transport behaviors, it was speculated that the optimal performance could be achieved by FDMs-P-AD, where the A side served as the water supplier and the D side was the solar

absorber (Fig. 4a). Moreover, the SEM images implied that the superstructure maintained in the FDMs-P and the array-pores were not blocked after Ppy coating (Supplementary Fig. S23). The ultraviolet-visible-near-infrared (UV-Vis-NIR) absorption spectra were illustrated in Fig. 4b. Among them, the D side of FDM-1-P, i.e., FDM-1-P (D) presented a higher light absorption rate of 93.19% than the A side of FDM-1-P, i.e., FDM-1-P (A) (85.27%). Similar results were also obtained for FDM-2-P (85.91% for the A side and 93.72% for the D side), which confirmed the larger absorption area of the D side without macropores. The real-time surface temperatures of the evaporators under one sun illumination were recorded by an infrared camera (IR). As shown in Fig. 4c, the average surface temperatures of all evaporators reached equilibrium within ~3 mins, indicating the rapid photothermal response. Since the D side had better light absorption and heat concentration, the FDMs-P-AD exhibited higher temperatures of ~6 °C than those of the FDMs-P-DA (Supplementary Fig. S24a). However, their temperatures were slightly lower than those of the CMMs-P (Supplementary Fig. S24b), due to the faster evaporation of FDMs-P-AD that carried more heat away on the surface.

Evaporation experiments were carried out through the device shown in Figs. S2–5. The membrane sample was placed on absorbent paper-wrapped polystyrene (PS) foam, which floated on the water surface to ensure a continuous water supply. A xenon lamp was used to simulate sunlight irradiation, while a balance connected to a computer recorded the real-time mass changes. The mass changes of different membrane evaporators were collected to calculate the evaporation rate. Besides, the energy conversion efficiency was obtained (Supplementary Methods S3 and Method S4). As shown in Fig. 4d and Supplementary Fig. S26, compared to pure water ($0.23 \text{ kg m}^{-2} \text{ h}^{-1}$), all evaporators exhibited significantly improved evaporation rates under 1 sun radiation. Among them, the FDMs-P-AD displayed a higher evaporation rate and energy efficiency than FDMs-P-DA, corresponding to the results of directional water transport and photothermal conversion tests. Particularly, the FDM-2-P-AD possessed the highest evaporation rate of $2.03 \text{ kg m}^{-2} \text{ h}^{-1}$ and efficiency of 94.54%, respectively, better than FDM-1-P-AD ($1.90 \text{ kg m}^{-2} \text{ h}^{-1}$ and 91.24%, respectively) and superior to CMMs-P ($1.43 \text{ kg m}^{-2} \text{ h}^{-1}$ and 78.27% respectively for CMM-1-P, $1.57 \text{ kg m}^{-2} \text{ h}^{-1}$ and 82.81%, respectively, for CMM-2-P) (Fig. 4e). Although both the FDM-1-P and FDM-2-P possessed superstructures that benefited ISE, the performances existed fine distinction for the following reasons. On one hand, the highly interconnected and continuous sponge-like gradient pores in the FDM-2-P were more advantageous than finger-like gradient pores in the FDM-1-P for constant water uptake and transport, for the reason that the finger-like cavities in FDM-1-P were much larger than the sponge-like pores in FDM-2-P. According to the capillary formula^{29,30}, the smaller and more continuous pores in FDM-2-P facilitated higher capillary-driven ascent, thus benefiting the anti-gravity water transport (Supplementary Movie S2 and 3). In contrast, for FDM-1-P, the capillary effect was not that obvious in the larger cavities. To further explain this phenomenon, finite element simulations were conducted to investigate the capillary-driven transport behavior of water molecules within channels of varying gradient pore sizes (Supplementary Fig. S27). The simulation results indicated that in smaller pore channels, water molecules exhibited faster transport rates upwards, consistent with the results of our anti-gravity water transport experiments and theoretical predictions. On the other hand, these tubular cavities impeded vertical heat conduction more severely, thereby triggering greater heat loss. In addition, many secondary pores on the A side of FDM-2-P afforded more capillary channels for water uptake. It hence highlighted the structural superiority of FDM-2-P according to the structure-function relationship of monolayered membranes. We also analyzed the Raman experiment to evaluate the states of water in FDM-2-P. From the Raman spectra (Supplementary Figs. S28–31), there were two bands derived at 3449 and 3610 cm^{-1} , attributed to the intermediate water (IW)^{31–33}.

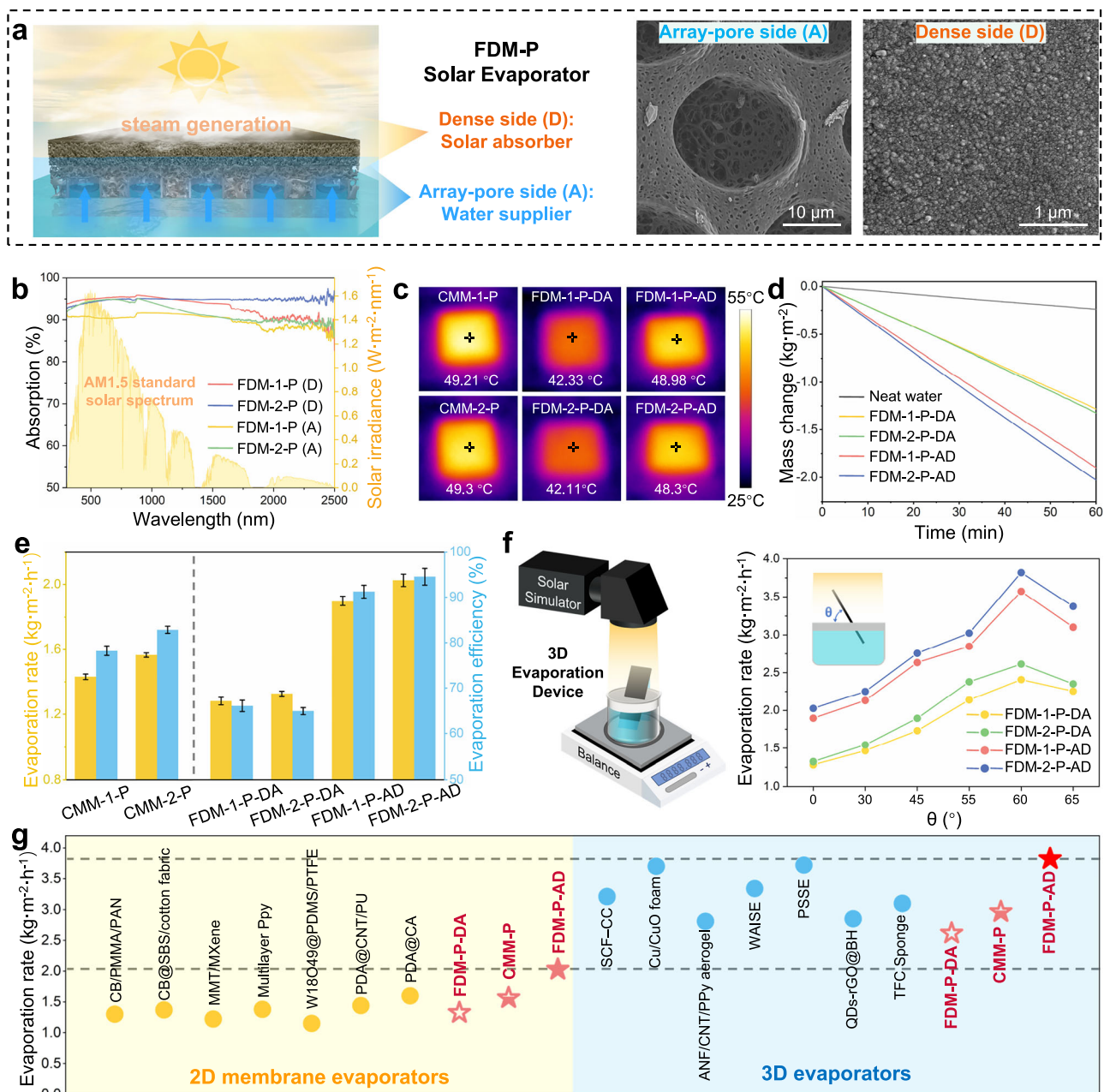


Fig. 4 | Photothermal conversion ability and solar evaporation performance. **a** Schematic illustration of the FDMs-P-AD and the SEM Images of both sides. **b** UV-Vis-NIR spectra of FDMs-P. **c** IR images showing the temperature distribution of the evaporators. **d** Mass changes of evaporators during evaporation under 1.0 kW m^{-2} solar radiation. **e** Evaporation rate and energy conversion efficiency of evaporators.

Data are shown as mean \pm SD ($n = 3$ independent experiments). **f** Schematic illustration of the 3D evaporation device and the dependence of evaporation rate on the tilt angle of the FDMs-P in the 3D evaporation device. **g** Comparison of the evaporation rate between FDMs-P-AD and other evaporators. Source data are provided as a Source Data file.

Although the FDMs-P-AD presented excellent evaporation performance among two-dimensional (2D) membrane materials and the energy loss was relatively low (calculated through Supplementary Method S5), there still remained some gaps with currently reported 3D evaporators. This is because the evaporation primarily occurred at the horizontal liquid-air interface for membrane materials, rather than vertical direction. 3D monolithic materials can possess larger evaporation volumes, thus allowing more water vapor to escape into the air multi-dimensionally and therefore resulting in higher evaporation rates than 2D cases. Thus, to break the limit of dimension, we established a 3D evaporation device (Supplementary Fig. S32) based on FDMs-P-AD to further expand the spatial utilization as well as the evaporation performances^{34,35}. As shown in Fig. 4f, the

evaporation rate was enhanced with the decreased projection area from the increased tilt angles at first. It can reach a maximum value of $3.82 \text{ kg m}^{-2} \text{ h}^{-1}$ for FDM-2-P-AD at 60° . Nevertheless, a larger tilt angle at 65° caused a slight decrease in the evaporation rate, originating from the less-sufficient water supply. Interestingly, in this configuration, all the FDMs-P-AD showed larger evaporation rates than FDMs-P-DA as well, conforming to the tendency of 2D cases. Finally, the ISE performances of FDM-2-P-AD were compared among currently reported 2D and 3D evaporators^{8,34–46}. As a monolayered 2D membrane evaporator, the evaporation rate of FDM-2-P-AD surpassed most 2D evaporators^{8,35–40}. Notably, when configured as a 3D evaporator, it achieved performance comparable to other advanced 3D evaporators^{34,41–46} (Fig. 4g).

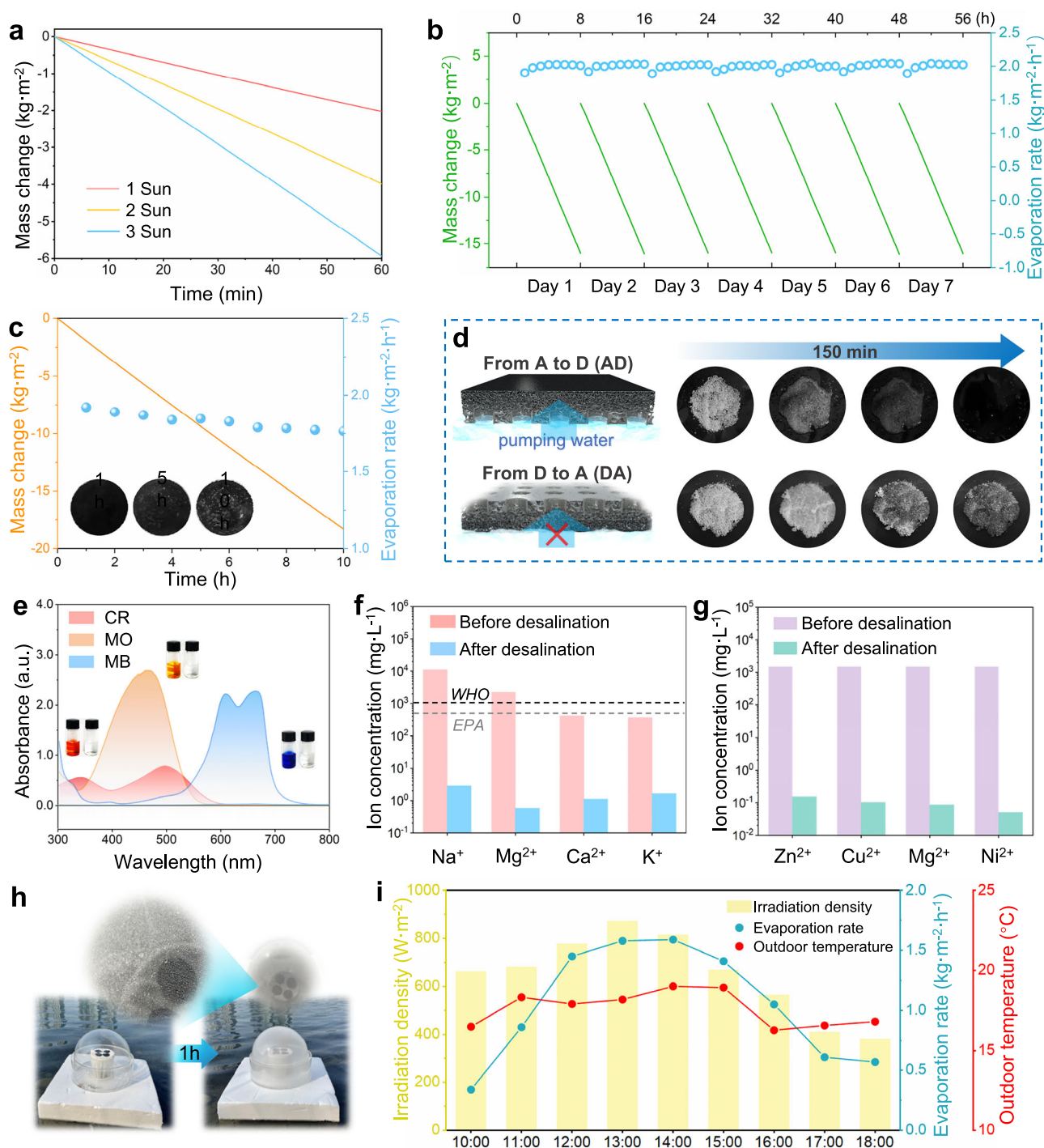


Fig. 5 | Practicability of FDMs-based evaporators. a Mass changes of FDM-2-P-AD under 1, 2, and 3 sun. **b** Mass change and evaporation rate of FDM-2-P-AD during long-term cyclic evaporation experiment. **c** Long-term evaporation experiments in 3.5 wt% brine. The inset photos demonstrate the little salt crystallization on the membrane evaporator surface during 10-hour evaporation. **d** The salt dissolution experiment of the FDM-2-P evaporator. **e** UV absorbance (a.u.: arbitrary units) and digital photos of different dyes before and after purification. **f** Concentration of salt

ions in simulated seawater before and after purification. **g** Concentration of heavy metal ions in aqueous solution before and after purification. **h** Digital photos of the homemade outdoor evaporation device floating on open water. A magnified view shows that generated water vapor nucleates into discrete liquid droplets. **i** Solar intensity, evaporation rate, and temperature for outdoor evaporation experiments from 10:00 to 18:00 in Chengdu, Sichuan Province, China. Source data are provided as a Source Data file.

To prove the practicability, the FDM-2-P-AD was selected for further tests of durability and purification capabilities. As shown in Fig. 5a, the evaporation rate was approximately proportional to the sunlight intensity under 1, 2, and 3 sun illumination, maximum arriving at $5.93 \text{ kg} \cdot \text{m}^{-2} \cdot \text{h}^{-1}$. The results reflected that the water supply was sufficient in the evaporator, which could adaptively maintain a suitable internal water volume. Long-term cyclic evaporation was conducted to

test the stability. The evaporation rate kept steady between 1.89 and $2.08 \text{ kg} \cdot \text{m}^{-2} \cdot \text{h}^{-1}$ under 1 sun illumination, and no sudden decrease was observed for 1 week (Fig. 5b). Next, the salt resistance was measured. We conducted long-term evaporation in 3.5 wt% brine. After 10 hours, the evaporation rate can maintain ~90% (Fig. 5c). This stability arose from the membrane's asymmetric pore-gradient design, where the arrayed macropores at the bottom facilitated rapid water supply while

the nanopores on the upper surface generated directional capillary flow to sustain evaporation and suppressed salt accumulation. Additionally, the upper dense side acted as a barrier to limit upward salt transport, enabling dynamic salt-water balance through continuous ion diffusion. The inset photographs confirmed the excellent salt resistance and evaporation stability by showing that only a small amount of salt crystals precipitated on the surface of FDM-2-P-AD. More importantly, the fabricated evaporator exhibited a self-cleaning capability to spontaneously re-dissolve the residual salt crystals into the brine (Fig. 5d). It was ascribed to the diode-like water transport property to allow the FDM-2-P-AD rapid recovery of evaporation activity. Then, the purification capability for water remediation was evaluated by various models. As shown in Fig. 5e, the solutions of Congo Red, Methyl Orange, and Methyl Blue with a concentration of 50 mg L⁻¹ were prepared to simulate organic pollutants in wastewater for evaporation experiments. After distillation, the solutions of all three dyes became colorless. No absorbance bands were identified, suggesting no dye residuals in the purified water. Furthermore, simulated seawater was used to validate the desalination capability (Fig. 5f). After purification, the concentrations of ions (Na⁺, K⁺, Mg²⁺, and Ca²⁺) in seawater drastically decreased by 3–4 orders of magnitude compared to the pristine levels. Meanwhile, the concentration of Na⁺ was below the salinity levels specified by the World Health Organization (WHO) and the Environmental Protection Agency (EPA) standards⁴⁷. In addition, various heavy metal ions were selected to simulate industrial wastewater in Fig. 5g. After purification, the concentrations of the ions (Mg²⁺, Zn²⁺, Ni²⁺, and Cu²⁺) in the simulated wastewater sharply reduced from 1500 to 0.086, 0.151, 0.050, and 0.102 mg L⁻¹, respectively, below the levels specified in the drinking water standard (GB5749-2006). Furthermore, considering the potential impact of microorganisms in wastewater on evaporator stability, we conducted light-induced antibacterial tests to validate the self-antibacterial capability of FDM-2-P. The membranes were co-cultured with *E. coli* and *S. aureus* suspensions (10⁶ CFU/mL) under both light and dark conditions. As shown in Supplementary Fig. S33, the 1-sun illuminated membranes achieved >99.9% bacterial clearance rates for both strains, thereby proving the good antibacterial property. Finally, the outdoor evaporation experiments were carried out on the lake of Donghu Park in Chengdu, China, from 10:00 to 18:00 on 19 October 2023. As illustrated in Supplementary Fig. S34, a homemade water purification device was floated on the expansive water surface. After 1 h, the generated steam was observed to condense on the inner wall of the device shell. (Fig. 5h) Meanwhile, the purified water flowed down for collection. The evaporation rate, temperature, and solar radiation intensity during this period were recorded accordingly (Fig. 5i). The average temperature during this period was 17.6 °C, and the average solar radiation intensity was 648.4 W m⁻². Even in this cool autumn, the device still produced 6.13 kg m⁻² of purified water within a day (8 hours), which was higher or comparable to many reported evaporators^{35,48,49}. Additionally, on account of the average solar radiation and the measured evaporation rate indoors, we estimated the collection efficiency of vapor-condensed water during this outdoor experiment to be ~58%.

Hydrovoltaic performances of FDMs

In addition to ISE, the diode-like water transport of the FDMs-P can be advantageous and applicable to many other fields. For example, current research focused on the potential of utilizing solar evaporators to simultaneously generate electricity through the hydrovoltaic effect^{50,51}. Building on this concept, we developed a straightforward electricity generator based on FDMs-P-AD. As shown in Fig. 6a, the FDMs-P-AD is sandwiched between indium-tin-oxide-coated polyethylene terephthalate (ITO-PET) electrodes to collect the electricity. Through zeta potential measurement, the FDMs-P were negatively charged (Supplementary Fig. S35), originating from the sulfone group of the polymer substrate. According to the literature⁵², when the nanochannel was

touched by the water, an overlapping electrical double layer formed on the nanochannel surface where the anions were repelled. Meanwhile, the cations passed through and accumulated at the top of the nanochannel. Consequently, it generated a streaming current. In our case, because of the asymmetric structure and gradient pore channels for the directional acceleration of water transport, when water and moisture entered the FDM from the A side, more cations flew upwards to the D side and thereby created a potential difference between the A and D sides. Thus, the FDMs-P-AD can generate a larger potential difference than the CMMs-P did (Fig. 6b). Particularly, for FDM-2-P-AD, an open-circuit voltage (V_{oc}) exceeding 200 mV was achieved in an ambient environment, which was the highest among all samples. Likewise, it also showed the highest short-circuit current (I_{sc}) (Fig. 6c). Besides, the FDM-2-P-AD was capable of steadily outputting voltage and current over a certain period (Fig. 6d). Connecting the devices in series derived a regular increase in voltage output (Fig. 6e), maximally reaching over 1.6 V in a series of seven units. Moreover, the tandem devices were practical to power some electronics, such as e-watch (Fig. 6f) and a light-emitting diode (Supplementary Fig. S36). Thus, the optimized energy generation capability highlighted the elegant structural design of the FDMs-P.

Discussion

In summary, we designed a class of flexible and robust FDMs via a facile PCTA strategy. The superstructure design offered a topological asymmetry and pore hierarchy to substantially modulate the water transport behavior. For ISE, the FDM-2-P-AD endowed a high evaporation performance with an evaporation rate of maximally 3.82 kg m⁻² h⁻¹ and an evaporation efficiency of 94.54% under 1 sun illumination, which were extraordinary among current membrane evaporators. Additionally, the excellent durability, salt resistance and contaminants purification performances, together with the outdoor evaluation, validated the practicability of FDM-based evaporators. Moreover, the diode-like water transport property of FDMs-AD configuration can be further extended to magnify the hydrovoltaic effect for power generation. Going beyond industrial deployment of FDMs via PCTA strategy can be envisioned by adopting low-cost durable templates, precise control of micro-patterning, and integration of casting-phase separation-demolding processes. Hence, this work addressed the trade-off between water supply and heat localization in membrane evaporators as well as avoiding interfacial issues in multi-layered evaporators, which paved the way for advanced membranes in environmental and energy-related applications.

Methods

Materials

Polyethersulfone (PES, Ultrason E6020P) and Polyvinylpyrrolidone (PVP-K16-18, PVP-K85) were obtained from BASF (Germany). N, N-Dimethylacetamide (DMAC) was purchased from Chengdu Kelong Chemical Co., Ltd (China). Pyrrole (99%), Congo Red (CR), Methyl Orange (MO) and Methylene Blue (MB) were purchased from Aladdin Reagent Co. (Shanghai, China). FeCl₃·6H₂O (99%) NaCl (99.9%), CaCl₂ (96.0%), MgSO₄ (98.0%), CuSO₄ (98.5%), ZnCl₂ (98.0%), and NiSO₄·6H₂O (98.5%) were provided by Greagent. ITO-PET was purchased from Sigma-Aldrich. Deionized water was obtained by a water purifier (UL Pure KE0119). All reagents were used as purchased without further purification.

Preparation of FDMs and CMMs

FDMs were fabricated through a PCTA strategy. The precursor formulations were precisely controlled: for FDM-1 and CMM-1, the solution comprised 17 wt% PES and 5 wt% low-molecular-weight PVP (K16-18) in DMAC, while FDM-2 and CMM-2 contained 17 wt% PES, 3.5 wt% high-molecular-weight PVP (K85), and 6 wt% H₂O in DMAC. According to these ratios, PES and PVP solution was stirred and

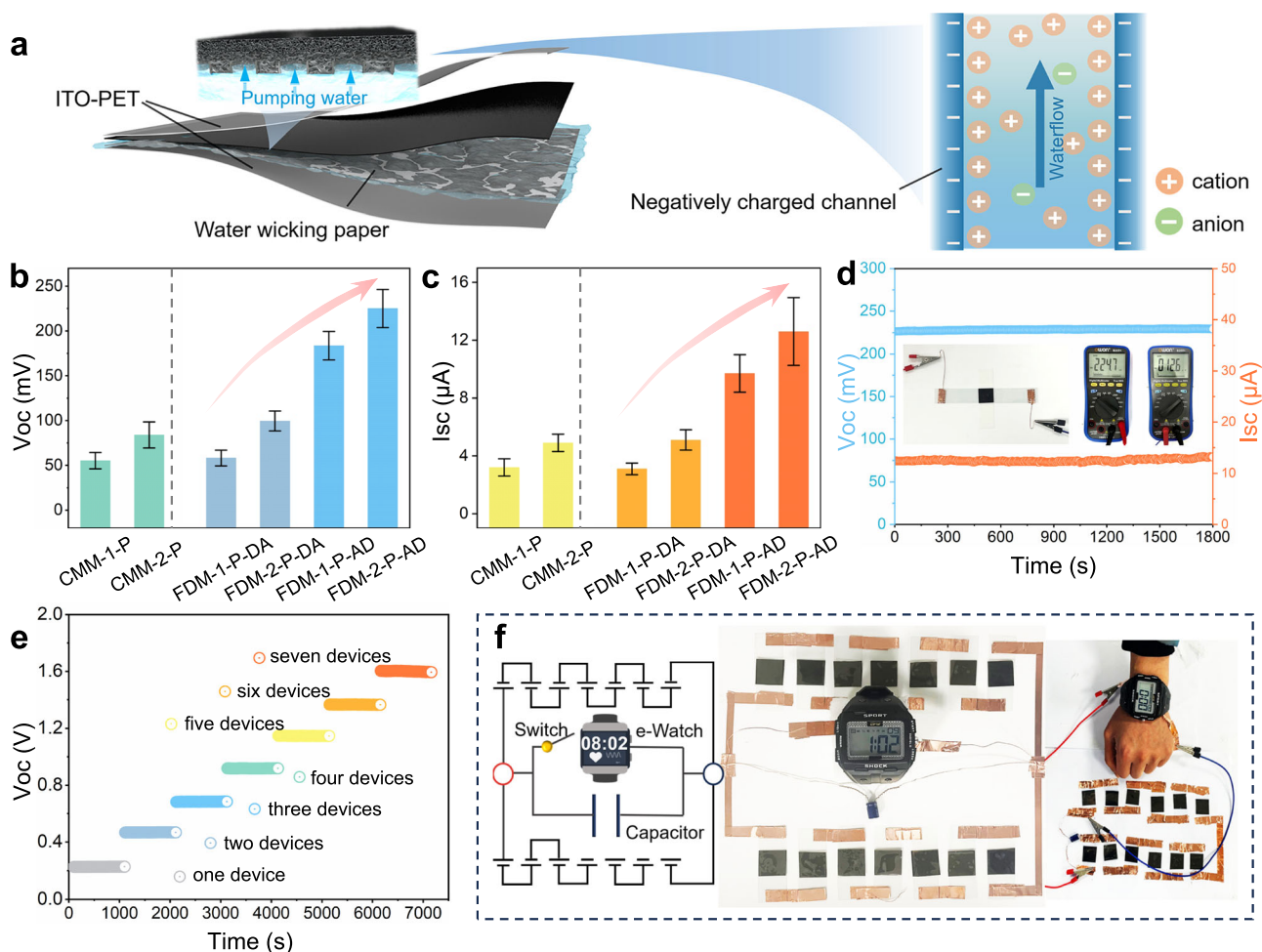


Fig. 6 | Hydrovoltaic applications. **a** Schematic depiction of the working mechanism of the flexible hydrovoltaic device based on the FDMs-P-AD. **b** Output voltage (V_{oc}) and **(c)** shortcircuit current (I_{sc}) of the membranes-based hydrovoltaic devices. Data are shown as mean \pm SD ($n = 3$ independent experiments). **d** V_{oc} and

I_{sc} of FDM-2-P-AD hydrovoltaic device as a function of time. **e** V_{oc} of FDM-2-P-AD hydrovoltaic devices connected in series. **f** Demonstration of powering a digital watch by connecting the energy generators in series and parallel, and the equivalent circuit. Source data are provided as a Source Data file.

dissolved in DMAC until a homogeneous and transparent solution was obtained. The solution was allowed to stand for 24 hours to remove bubbles. Subsequently, the solution was spin-coated onto a silicon wafer template with array patterns. For FDM-1, the spin-coating speed was set to be 700 rpm and the coating time was 8 s. While for FDM-2, the spin-coating speed was set to be 500 rpm for 20 s, followed by 1000 rpm for 10 s. Afterwards, it was immersed in deionized water for 12 hours to solidify the membrane and rinse off excess PVP with deionized water. CMMs were fabricated by a similar method, except that the glass plates were used instead of a silicon wafer template. The as-prepared membranes were stored in DI water for use.

Preparation of FDMs-P and CMMs-P

The preparation of FDMs-P and CMMs-P was enabled through the vapor polymerization of Ppy. Briefly, the FDM was immersed in an ethanol solution of $FeCl_3 \cdot 6H_2O$ (0.25 mol L^{-1}) (oxidant) for 2 hours, followed by air-drying. Then, the $FeCl_3$ -impregnated membrane was placed above the liquid pyrrole monomer in a sealed container, where the pyrrole was volatilized and the membrane was fully exposed to the vapor phase. The polymerization was carried out overnight at $4^\circ C$ in a closed container. After polymerization, the black membrane was washed with water and ethanol for several times to utterly remove the unreacted oxidant, pyrrole monomer and byproducts. Finally, the as-obtained membranes were dried in air.

Characterization

The morphology characterizations were performed by scanning electron microscopy (SEM, Regulus8220, Japan) with Energy dispersive X-ray (EDX, Octane Elect Super, EDAX, U.S.A.). A 3D profilometer (Veeo Contour GT-K1) was employed to observe the surface topography. A FT-IR spectrometer (Nicolet-6700, USA) was utilized to analyze the structural composition of the samples. XPS experiments were conducted on an ESCALab250Xi using monochromatic $Al K\alpha$ X-rays with $h\nu = 1486.6 \text{ eV}$. UV-visible absorption spectra were recorded with a spectrophotometer (UV 3600I plus). Contact angles of the membranes were measured by using a contact angle tester (Kruss DSA100, Germany). Raman spectra were recorded by a micro confocal laser Raman spectrometer with a 532 nm exciting wavelength (HR Evolution). Differential scanning calorimetry (DSC) measurements were conducted by METTLER DSC3. Metal ions in the solution were determined by inductively coupled plasma spectrometry (ICP-MS, Perkin Elmer, Optima 8300).

Water transport experiments

For macroscopic observation, a Congo Red dye solution droplet was carefully deposited on the membrane surface to observe its wettability behavior, namely, whether it remained pinned or spread out. For evaluating the anti-gravity water transport ability, a water contact angle instrument equipped with a camera was employed. The FDM was fixed with one side facing down, and a droplet of water was placed on a hydrophobic substrate. The droplet was brought into contact with the

membrane sample from below, and the entire process was recorded for analysis.

For microscopic observation, a 0.5 M copper ion aqueous solution was prepared as a contrast agent. The contrast agent was applied to either A or D side of the membrane, followed by drying naturally. Subsequently, micro computed tomography (micro CT) was used to observe the internal morphology of the membrane samples. Regions reached by the contrast agent presented bright spots, enabling the evaluation of water transport from different directions through the membrane.

Water evaporation experiments

Water evaporation was measured based on the mass loss of water using an electronic balance (FA224). In summary, the membrane sample was in direct contact with polystyrene (PS) foam wrapped in absorbent paper, which floated on the water surface. The absorbent paper helped provide a continuous water supply. Additionally, the PS foam served as thermal insulation to minimize heat transfer loss and maintain heat at the interface. A xenon lamp light source was used to simulate vertical sunlight irradiation on the sample surface, and a balance was connected to a computer to record the mass change in real-time. For the setup of the 3D evaporation device, the membrane samples were cut into strips of 40 mm × 15 mm, tilted at an angle, and placed under a xenon lamp for illumination. Their projection area was used to calculate the evaporation rate.

Salt resistance evaluation

The salt resistance of the evaporators was evaluated through dynamic evaporation and self-cleaning experiments. For the dynamic evaporation test, a 3.5 wt.% NaCl aqueous solution (simulating seawater salinity) was used as the feed under 1-sun illumination. The mass change of the solution was monitored in real-time using a high-precision balance (± 0.1 mg), and the evaporation rate was calculated from the mass loss curve. Simultaneously, the membrane surface was observed over time to detect potential salt crystallization during the evaporation process. To further assess the self-cleaning capability, a separate experiment was conducted under no solar illumination to eliminate photothermal effects. Specifically, 1.0 g of NaCl crystals were uniformly dispersed on the membrane surface. The system was then exposed to ambient humidity without external rinsing. The spontaneous dissolution and migration of salt particles were tracked through optical imaging.

Multifunctional water remediation tests

Firstly, 50 mg/L solutions of CR, MO, and MB were prepared respectively as typical pollutants to characterize the dye wastewater purification capability of the samples. To assess the desalination capability of samples, simulated seawater was prepared by thoroughly mixing 24.53 g of NaCl, 11.09 g of MgSO_4 , 4.09 g of Na_2SO_4 , 1.16 g of CaCl_2 , 0.70 g of KCl, and 0.20 g of NaHCO_3 with 1 L of water until fully dissolved through agitation. Using MgSO_4 , CuSO_4 , ZnCl_2 , and $\text{NiSO}_4 \cdot 6\text{H}_2\text{O}$ raw materials, four different ion solutions of Mg^{2+} , Cu^{2+} , Zn^{2+} , and Ni^{2+} were prepared to simulate heavy metal wastewater and then evaluate the purification capacity of the samples. The prepared solutions mentioned above were used instead of pure water for evaporation experiments. The purification capability was assessed by collecting condensed water and characterizing the changes in composition between the condensed water and the original solution.

Hydrovoltaic electricity generation experiments

To collect the electricity from the hydrovoltaic effect, the membrane was sandwiched between ITO-PET electrodes. Electricity generation performances (including voltage and current) were recorded via a digital multimeter (OWON B35T). In addition, a 1 farad capacitor was used to store and release the generated current of FDMs-P devices to support the electronic devices.

Data availability

All data supporting the findings of this study are available in the article, the Supplementary Information and the Source Data file. Source data are provided with this paper.

References

- Lewis, N. S. Research opportunities to advance solar energy utilization. *Science* **351**, aad1920 (2016).
- Zhao, F., Guo, Y., Zhou, X., Shi, W. & Yu, G. Materials for solar-powered water evaporation. *Nat. Rev. Mater.* **5**, 388–401 (2020).
- Ghasemi, H. et al. Solar steam generation by heat localization. *Nat. Commun.* **5**, 4449 (2014).
- Zhou, X., Zhao, F., Zhang, P. & Yu, G. Solar water evaporation toward water purification and beyond. *ACS Mater. Lett.* **3**, 1112–1129 (2021).
- Tao, P. et al. Solar-driven interfacial evaporation. *Nat. Energy* **3**, 1031–1041 (2018).
- Zhao, F. Highly efficient solar vapour generation via hierarchically nanostructured gels. *Nat. Nanotechnol.* **13**, 489 (2018).
- Chen, Z. et al. Janus nano-micro structure-enabled coupling of photothermal conversion, heat localization and water supply for high-efficiency solar-driven interfacial evaporation. *Adv. Funct. Mater.* **33**, 2303656 (2023).
- Xu, W. et al. Flexible and salt resistant janus absorbers by electro-spinning for stable and efficient solar desalination. *Adv. Energy Mater.* **8**, 1702884 (2018).
- Zhou, X., Zhao, F., Guo, Y., Zhang, Y. & Yu, G. A hydrogel-based antifouling solar evaporator for highly efficient water desalination. *Energy Environ. Sci.* **11**, 1985–1992 (2018).
- Yao, H. et al. Janus-interface engineering boosting solar steam towards high-efficiency water collection. *Energy Environ. Sci.* **14**, 5330–5338 (2021).
- Lu, H. et al. High-yield and low-cost solar water purification via hydrogel-based membrane distillation. *Adv. Funct. Mater.* **31**, 2101036 (2021).
- Guo, Y. & Yu, G. Materials innovation for global water sustainability. *ACS Mater. Lett.* **4**, 713 (2022).
- Wei, D. et al. Enabling self-adaptive water-energy-balance of photothermal water diode evaporator: dynamically maximizing energy utilization under the ever-changing sunlight. *Adv. Mater.* **36**, 2309507 (2024).
- Li, H. et al. Self-assembled nanofibrous hydrogels with tunable porous network for highly efficient solar desalination in strong brine. *Adv. Funct. Mater.* **33**, 2308492 (2023).
- Tian, X., Li, J. & Wang, X. Anisotropic liquid penetration arising from a cross-sectional wettability gradient. *Soft Matter* **8**, 2633–2637 (2012).
- Zhang, Q. et al. Highly flexible monolayered porous membrane with superhydrophilicity–hydrophobicity for unidirectional liquid penetration. *ACS Nano* **14**, 7287–7296 (2020).
- Shiohara, A., Prieto-Simon, B. & Voelcker, N. H. Porous polymeric membranes: fabrication techniques and biomedical applications. *J. Mater. Chem. B* **9**, 2129–2154 (2021).
- Zhou, X., Guo, Y., Zhao, F. & Yu, G. Hydrogels as an emerging material platform for solar water purification. *Acc. Chem. Res.* **52**, 3244–3253 (2019).
- Chen, C., Kuang, Y. & Hu, L. Challenges and opportunities for solar evaporation. *Joule* **3**, 683–718 (2019).
- Xia, Q. et al. Solar-driven abnormal evaporation of nanoconfined water. *Sci. Adv.* **10**, ead3760 (2024).
- Hu, X. & Zhu, J. Tailoring aerogels and related 3D macroporous monoliths for interfacial solar vapor generation. *Adv. Funct. Mater.* **30**, 1907234 (2020).
- Chen, P., Zhong, W. & Ai, B. Separation of biological ion in asymmetric nanochannels through alternating electric field. *J. Stat. Mech.* **2018**, 083203 (2018).

23. Ai, B.-Q., He, Y.-F. & Zhong, W.-R. Entropic Ratchet transport of interacting active Brownian particles. *J. Chem. Phys.* **141**, 194111 (2014).
24. Zhang, L. et al. Rheological behavior of PES/PVP/DMAc solution and PVP structural regulation for hollow fiber membrane. *J. Appl. Polym. Sci.* **139**, e52870 (2022).
25. Dong, X., Lu, D., Harris, T. A. L. & Escobar, I. C. Polymers and solvents used in membrane fabrication: a review focusing on sustainable membrane development. *Membranes* **11**, 309 (2021).
26. Qian, Y., Xue, G., Chen, L., Xu, G. & Wang, G.-E. Conductive metal-organic framework nanosheets constructed hierarchical water transport biological channel for high-performance interfacial seawater evaporation. *Adv. Mater.* **36**, 2310795 (2024).
27. He, G.-Y., Tsao, H.-K. & Sheng, Y.-J. Capillary flow in nanoporous media: effective Laplace pressure. *Colloids Surf. A Physicochem. Eng. Asp.* **699**, 134499 (2024).
28. Yang, H.-C. et al. Janus membranes: creating asymmetry for energy efficiency. *Adv. Mater.* **30**, 1801495 (2018).
29. Dai, C. et al. Strategic design of porous interfacial evaporators: a comprehensive review unveiling the significant role of pore engineering. *Nano Energy* **131**, 110244 (2024).
30. Zhang, J. et al. Water distribution modelling of capillary absorption in cementitious materials. *Constr. Build. Mater.* **216**, 468–475 (2019).
31. Zhou, X., Zhao, F., Guo, Y., Rosenberger, B. & Yu, G. Architecting highly hydratable polymer networks to tune the water state for solar water purification. *Sci. Adv.* **5**, eaaw5484 (2019).
32. Guo, Y. et al. Biomass-derived hybrid hydrogel evaporators for cost-effective solar water purification. *Adv. Mater.* **32**, 1907061 (2020).
33. Wei, D. et al. Water activation in solar-powered vapor generation. *Adv. Mater.* **35**, 2212100 (2023).
34. Liu, X. et al. An easy-to-fabricate 2.5D evaporator for efficient solar desalination. *Adv. Funct. Mater.* **31**, 2100911 (2021).
35. Chang, Y. et al. Hydrophobic W18O49 mesocrystal on hydrophilic PTFE membrane as an efficient solar steam generation device under one sun. *J. Mater. Chem. A* **6**, 10939–10946 (2018).
36. Tian, Y. et al. Breath-figure self-assembled low-cost janus fabrics for highly efficient and stable solar desalination. *Adv. Funct. Mater.* **32**, 2113258 (2022).
37. Wang, X., Liu, Q., Wu, S., Xu, B. & Xu, H. Multilayer polypyrrole nanosheets with self-organized surface structures for flexible and efficient solar-thermal energy conversion. *Adv. Mater.* **31**, 1807716 (2019).
38. He, M., Liu, H., Wang, L., Qin, X. & Yu, J. One-step fabrication of a stretchable and anti-oil-fouling nanofiber membrane for solar steam generation. *Mater. Chem. Front.* **5**, 3673–3680 (2021).
39. Yang, Y. et al. A bioinspired antibacterial and photothermal membrane for stable and durable clean water remediation. *Mater. Horiz.* **10**, 268–276 (2023).
40. Ai, Z. et al. Floating MMT/MXene janus membrane for solar steam generation and mechanism of improving water transportation by DFT calculation. *Sep. Purif. Technol.* **300**, 121918 (2022).
41. Wu, S.-L. et al. Solar-driven evaporators with thin-film-composite architecture inspired by plant roots for treating concentrated nano-/submicrometer emulsions. *ACS Appl. Mater. Interfaces* **14**, 51555–51563 (2022).
42. Xie, Z., Zhu, J. & Zhang, L. Three-dimensionally structured polypyrrole-coated setaria viridis spike composites for efficient solar steam generation. *ACS Appl. Mater. Interfaces* **13**, 9027–9035 (2021).
43. Wang, C., Xu, K., Shi, G. & Wei, D. Water skin effect and arched double-sided evaporation for boosting all-weather high salinity desalination. *Adv. Energy Mater.* **13**, 2300134 (2023).
44. Wu, J. et al. Multifunctional solar evaporator with adjustable island structure improves performance and salt discharge capacity of desalination. *Adv. Sci.* **10**, 2305523 (2023).
45. Saleque, A. M., Al Subri Ivan, M. N., Ahmed, S. & Tsang, Y. H. Light-trapping texture bio-hydrogel with anti-biofouling and antibacterial properties for efficient solar desalination. *Chem. Eng. J.* **458**, 141430 (2023).
46. Wang, M. et al. Aramid-based aerogels for driving water evaporation through both photo-thermal and electro-thermal effects. *J. Mater. Chem. A* **11**, 7711–7723 (2023).
47. Li, Y. et al. Graphene oxide-based evaporator with one-dimensional water transport enabling high-efficiency solar desalination. *Nano Energy* **41**, 201–209 (2017).
48. Zhang, L. et al. Interfacial solar evaporation toward efficient recovery of clean water and concentration of nutrients from urine with polypyrrole-based photothermal conversion films. *Resour. Conserv. Recycl.* **188**, 106645 (2023).
49. Yang, P. et al. A melanin-inspired robust aerogel for multifunctional water remediation. *Mater. Horiz.* **10**, 1020–1029 (2023).
50. Zhang, Z. et al. Emerging hydrovoltaic technology. *Nat. Nanotech.* **13**, 1109–1119 (2018).
51. Zhang, Y. et al. Guaranteeing complete salt rejection by channeling saline water through fluidic photothermal structure toward synergistic zero energy clean water production and in situ energy generation. *ACS Energy Lett.* **5**, 3397–3404 (2020).
52. Li, L. et al. A flexible tough hydrovoltaic coating for wearable sensing electronics. *Adv. Mater.* **35**, 2304099 (2023).

Acknowledgements

J.W. acknowledges the financial support from the National Science Foundation of China (NSFC) (no. 52103178 and no. 52376063), the Sixth Two-hundred Talent B plan of Sichuan University. G.Y. acknowledges support from the Welch Foundation F-1861, Norman Hackerman Award in Chemical Research and Camille Dreyfus Teacher-Scholar Award. J.W. also sincerely thanks Professor Shudong Sun from Sichuan University for the discussions on this work.

Author contributions

J.W., M.A., C.Z., and G.Y. designed research; Y.C., P.Y., and J.W. performed research; Y.C., J.W., W.G., Z.L., and M.A. analyzed data; J.W., M.A., C.Z., W.G., and G.Y. wrote the paper.

Competing interests

The authors declare no competing interests.

Additional information

Supplementary information The online version contains supplementary material available at <https://doi.org/10.1038/s41467-025-60283-6>.

Correspondence and requests for materials should be addressed to Jiemin Wang, Meng An, Changsheng Zhao or Guihua Yu.

Peer review information *Nature Communications* thanks Ailin Gao and Tianxi Liu for their contribution to the peer review of this work. A peer review file is available.

Reprints and permissions information is available at <http://www.nature.com/reprints>

Publisher's note Springer Nature remains neutral with regard to jurisdictional claims in published maps and institutional affiliations.

Open Access This article is licensed under a Creative Commons Attribution-NonCommercial-NoDerivatives 4.0 International License, which permits any non-commercial use, sharing, distribution and reproduction in any medium or format, as long as you give appropriate credit to the original author(s) and the source, provide a link to the Creative Commons licence, and indicate if you modified the licensed material. You do not have permission under this licence to share adapted material derived from this article or parts of it. The images or other third party material in this article are included in the article's Creative Commons licence, unless indicated otherwise in a credit line to the material. If material is not included in the article's Creative Commons licence and your intended use is not permitted by statutory regulation or exceeds the permitted use, you will need to obtain permission directly from the copyright holder. To view a copy of this licence, visit <http://creativecommons.org/licenses/by-nc-nd/4.0/>.

© The Author(s) 2025